Chapter 12 – NUMERICAL SOLUTIONS FOR THE CAWAPI CONFIGURATION ON UNSTRUCTURED GRIDS AT BOEING-ST. LOUIS, UNITED STATES

by

Todd R. Michal, Matt Oser, Mortaza Mani and Frederick W. Roos

12.1 SUMMARY

Analyses performed with the Boeing Computational Fluid Dynamics code about the CAWAPI research aircraft at high angles of attack are presented. Results are compared with surface pressure and boundary layer measurements taken in flight. A sequence of investigations aimed at measuring the impact of grid resolution, grid topology, turbulence modelling and time accuracy on solution accuracy are described. Results from the studies are summarized in a collection of lessons learned to help guide future high angle of attack computations.

12.2 INTRODUCTION

Flight at high angle of attack is a critical part of the envelope for many of today's military aircraft and missile systems. Flight characteristics in this regime affect aircraft manoeuvrability, handling characteristics, stability and control, and safe store separation. High angle of attack flight is dominated by flow field features such as large areas of separation, complex vortical structures and unsteady flow. The ability to predict and understand the physics of these features enables them to be integrated into the vehicle design thereby improving performance.

Vehicle design in the high angle of attack regime has traditionally relied on empirical design methods and experience gained from previous designs. These methods provide a qualitative assessment of high-alpha characteristics but do not provide quantitative data on which to base a new vehicle design. Accurate data typically only becomes available late in the design process through wind-tunnel testing. Often this data becomes available too late to impact the vehicle design. In extreme circumstances, late discovery of adverse high-alpha interactions can lead to expensive program delays or program cancellation.

Computational Fluid Dynamic (CFD) simulation of high-alpha flows offers the possibility of providing quantitative data earlier in the design process. Unfortunately, the flow field features prevalent in high-alpha flight make accurate simulations in this environment challenging for today's CFD tools. Over the past several decades, steady progress has been made in modelling high alpha flows. Euler methods were shown to predict vortices on delta wings in the mid 1980's. The NASA High Angle of Attack Research Vehicle (HARV) program provided a wealth of test data for benchmarking CFD codes [12-1]. Several researchers compared structured CFD results against this data [12-2]. At Boeing, many programs have gained valuable data from CFD analysis of high angle of attack flows. Examples include assessment of tail buffet on the F/A-18C program and analysis of the booster separation aerodynamics for the Delta IV launch vehicle. For the most part these analyses were performed with structured grid methods and suffered from limited validation data upon which to verify the results. Structured grid CFD computations on complex vehicles can require several weeks or months to obtain, a time frame which severely limits their usefulness. Unstructured grid methods have demonstrated the ability to rapidly model and compute CFD data on complex configurations, but relatively little validation of unstructured grid methods has been performed for high-alpha flight.

A systematic study of CFD methods in the high-alpha flight regime is needed to quantify the accuracy, understand the best practices for modelling these flows, and increase the technology readiness of CFD for the next generation of fighter aircraft systems. This is particularly true for unstructured grid methods which have seen relatively little use in this flow field environment. In particular, a better understanding of the effect of unstructured grid discretization algorithms, turbulence modelling, and unstructured-grid topology and resolution requirements is needed.

In this chapter, data from the NASA Cranked Arrow Wing Aerodynamics Project is compared against the Boeing Computational Fluid Dynamics (BCFD) code. Results are presented from a series of computational studies. These studies were designed to investigate the impact of grid topology, grid resolution, solution algorithms and turbulence modelling. Comparisons with flight test data are used to assess the relative accuracy and formulate best practices for modelling high-alpha flow fields with the BCFD code.

12.3 CFD TOOLSET

The grids in this study were generated using the Boeing Modular Aerodynamic Computational Analysis Process (MADCAP). MADCAP was developed at Boeing as a modular framework to house grid generation capabilities from a variety of sources. MADCAP contains a fully automated surface mesh generation capability. In addition to the automated approach, the user can interactively control resolution and mesh element type through the selection of control nodes, edges and surfaces. Unstructured mesh algorithms can be selected from Boeing developed libraries and/or from the Advancing Front with Local Reconnection (AFLR) library [12-6]. Surface meshes can contain a combination of quadrilateral and triangular faces. The volume meshes used in this study were developed with the AFLR code using a combination of element types. Near the wall, advancing layers are used to place highly anisotropic prismatic elements across the boundary layer. Outside the boundary layer, isotropic tetrahedral elements are utilized. A smooth transition between the prismatic and tetrahedral elements is provided by growing each column of the boundary layer mesh until the element at the outside edge is nearly isotropic. The boundary layer resolution is controlled by specification of the initial spacing near the wall, an initial growth rate, a growth stretching and a maximum growth rate. In addition, the extent of the boundary layer thickness can be specified or an estimate of the boundary layer thickness for a turbulent flat plate can be used to extend the prismatic layers beyond the estimate. Control of the resolution of the tetrahedral portion of the mesh is provided by a linear interpolation from the surface mesh. Alternatively, the user can specify a geometry growth rate to control the stretching of resolution in the tetrahedral region. Sources in the form of individual nodes, curves or surfaces can be specified to control the off body resolution of the tetrahedral mesh.

The BCFD code is a general geometry and general purpose Euler and Navier-Stokes solver [12-7]. Any valid grid (structured, unstructured, and hybrid) can be utilized (tet, hex, prism, pyramid, and any mix of them) with the BCFD code. A mature second-order accurate zone coupling technique ensures continuity of the solution across zone boundaries. BCFD has an extensive library of boundary condition routines available on a point-by-point basis as well as various numerical algorithms such as Roe, HLLE, and Lax-Freidrichs/Rusanov. The default explicit spatial operator is a finite-volume second-order HLLE flux difference split scheme. Gradient reconstruction is performed at the cell centers and uses a total variation diminishing (TVD) limiter to improve robustness and convergence rate.

Turbulence models implemented in BCFD include the one-equation point-wise model of Goldberg, which does not require wall distance, and the one-equation Spalart-Allmaras (S-A) and two-equation Menter SST model, which utilize the wall distance. Also, the hybrid (RANS-LES) models SA/DES, SA/MDES, and SST/LESb , PRNS, and Detached-PRNS have been implemented.

BCFD incorporates a number of user-selectable (by zone) solution algorithms. The default time integration scheme is a first-order, implicit scheme where a point Gauss-Seidel with agglomeration multi-grid is used for unstructured grids. For steady-state flows, variable time steps based on local eigenvalues are used to speed convergence. For time-accurate calculation, BCFD offers a second-order Global Newton/dual-time algorithm which provides second-order accurate updates in the physical-time domain across all zones.

12.4 RESULTS

Studies were performed to investigate the impact of grid type, grid resolution and BCFD algorithmic options on solution accuracy about the F-16XL geometry. Flight Condition 7 was selected as the baseline condition for these studies because of the availability of both surface pressure and boundary layer data. All of the BCFD solutions presented in this chapter utilized the second-order accurate HLLE algorithm with TVD limiter.

Convergence of all BCFD solutions in this study was determined by monitoring the L2Norm of the residual of the solution variables and the overall integrated surface forces. A typical convergence history is shown in Figure 12-1. Because of the unsteady nature of the flow field, the surface forces did not converge to a steady value but rather they reached an oscillatory state about a mean value. It was found that reaching this oscillatory state was not an accurate prediction of convergence of the solution near the vortex core. To ensure full convergence, the surface pressure in the vicinity of the primary vortices was monitored as an additional gauge of solution convergence.

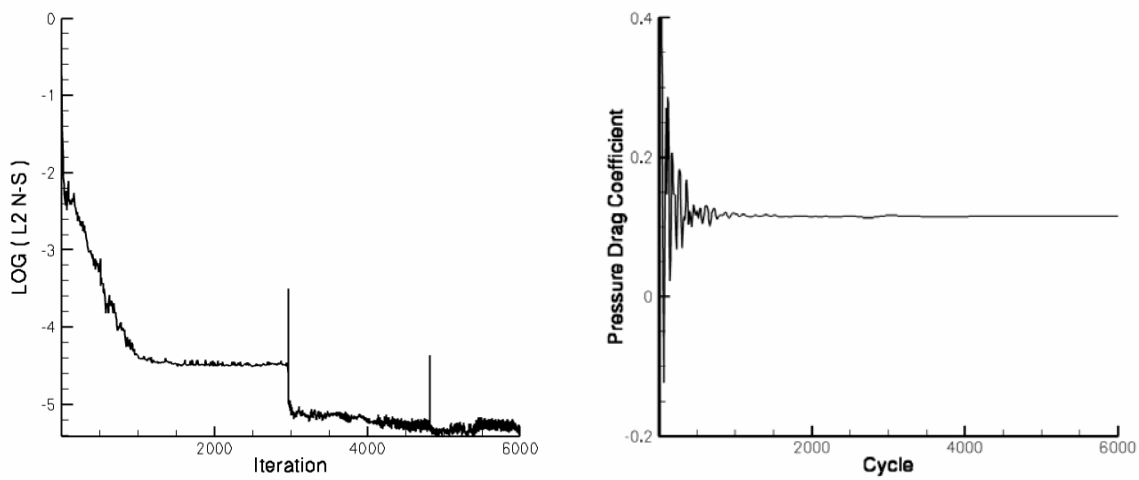

Figure 12-1: BCFD Convergence History from Sample AVT Solution.

The first study investigated the effect of grid resolution and cell topology on solution accuracy. A baseline solution was generated on the common unstructured grid supplied to the CAWAPI team members. This grid contains approximately 12 million volume elements. A complete description of the geometry and AVT common grid is provided in Reference [12-8]. The baseline BCFD solution was computed using the Spalart-Allmaras turbulence model and time integration to steady state was performed using 3 levels of multi-grid. Predicted contours of the surface pressure coefficient are shown in the left side of Figure 12-2. Cuts of the total pressure normalized by the free stream total pressure at several fuselage stations are shown in the right

side of Figure 12-3. The flow field is characterized by three primary vortices. The largest vortex forms at the root of the wing fuselage intersection and is fed by the flow around the 70 degree sweep inboard wing leading edge. About half way between the wing root and tip, the leading edge sweep suddenly changes to a sweep angle of 50 degrees. At this crank in the leading edge sweep, a second primary vortex is formed. Just inboard of the wing crank, there is a large vertical plate (fence) that limits communication between the inboard and outboard portions of the wing. A third primary vortex is generated at the leading edge of the fence and tracks on the outboard portion of the wing. Interactions between the inboard wing vortex and the fence play an important role in establishing the flow field.

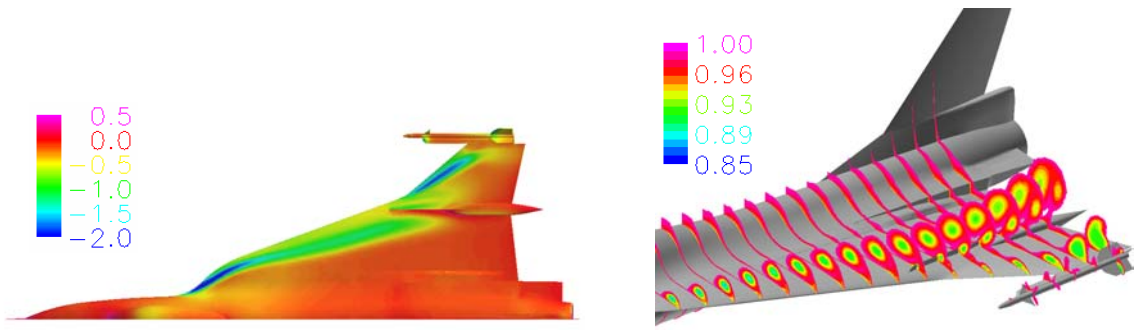

Figure 12-2: Surface Pressure Coefficient and Total Pressure Ratio Contours Computed on the Common Grid at Flight Condition 7.

Cuts of the computed surface pressure from all of the BCFD study results at butt-line (BL) stations of 55, 70, 80, 95 153.5 and 184.5 inches are shown in Figure 12-3. The BL locations BL are illustrated by solid red lines overlaid on top of the wing plan form for each plot. BL stations 55, 70 and 80 are located inboard of the fence and stations 153.5 and 184.5 are outboard of the fence. The BCFD solution on the common grid is indicated by the dot dash red line. The results follow the general trends of the test data, but consistently under predict the strength of the suction peak centered along the inboard and outboard vortex cores. The computed location of the suction peak is slightly forward of the test data. A second smaller suction peak upstream of the primary vortex indicating the location of a secondary vortex is clearly evident in the test data. In the BCFD common grid solution this secondary vortex is absent or marginally visible. The lack of a secondary vortex may be partially responsible for the offset of the primary vortex location in the common grid CFD results.

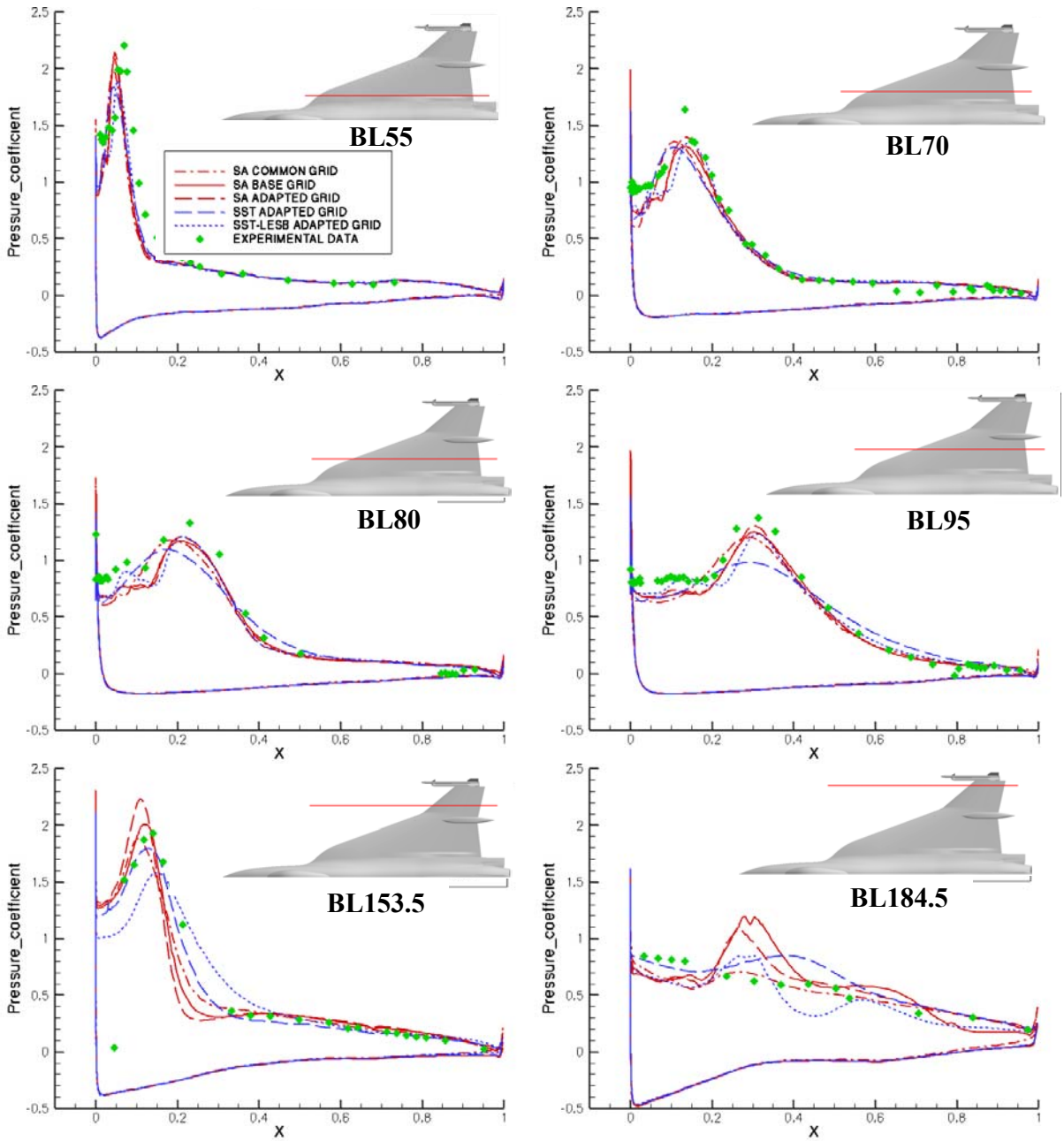

Figure 12-3: Comparison of Computed Surface Pressure Coefficient for Several Butt-Line Cuts at Flight Condition 7.

Predicted velocity profiles across the boundary layer at 4 rake locations are shown in Figure 12-4. The locations of the rakes are illustrated by the red dots on the plan form view with each plot. BCFD results computed on the common grid are indicated by the dot-dash red line in Figure 12-4. The predicted profiles show a lower gradient in the near wall region compared to the test data. The predicted profile is particularly far from the test data at rake location 7.

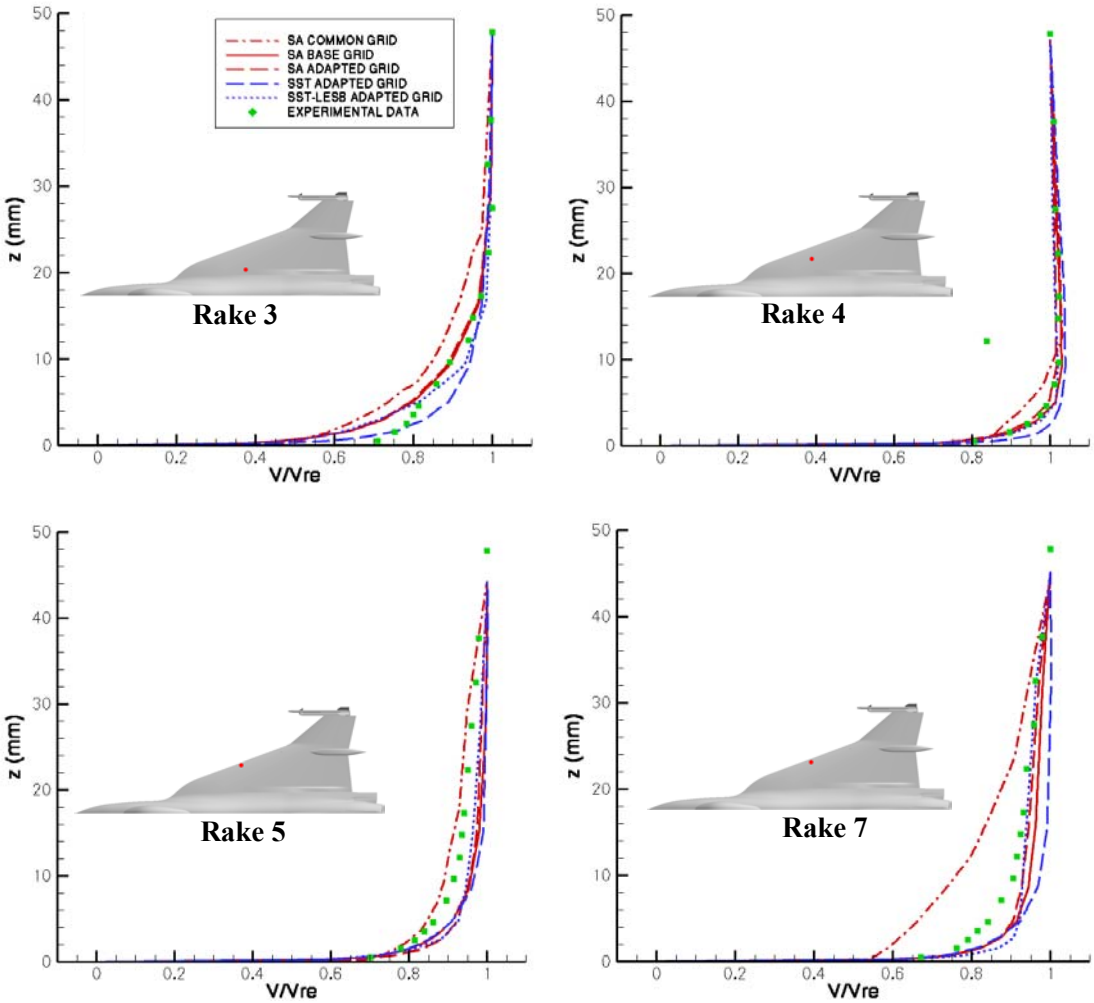

Figure 12-4: Comparison of Computed Velocity Profiles at Flight Condition 7.

One contributing factor to the lack of a secondary vortex in the CFD prediction may be the lack of adequate mesh resolution in the wing leading edge vortex region. The common mesh consists of an-isotropic triangular elements with an aspect ratio of about 10:1. The stream wise resolution at the leading edge is 0.228 inches resulting in about 10 faces circumferentially around the leading edge. The surface mesh near the wing leading edge is shown in Figure 12-5.

A mesh with higher-resolution was constructed in MADCAP to try and improve solution accuracy. In particular, the mesh was concentrated near the wing leading edge to try and improve the prediction near the secondary vortex. Mesh resolution was increased at the leading edge by introducing high aspect ratio quadrilateral elements into the surface mesh. The maximum aspect ratio of the quadrilateral faces is 25. The circumferential resolution at the leading edge is 0.05 inches inboard of the wing crank transitioning to 0.01 inch spacing near the wing tip. The quadrilateral elements were subdivided into triangles in the final mesh. A comparison of the Boeing and common meshes at the wing leading edge is shown in Figure 12-5. The resolution of the Boeing surface mesh is about double that of the common mesh in the immediate proximity of the wing vortices.

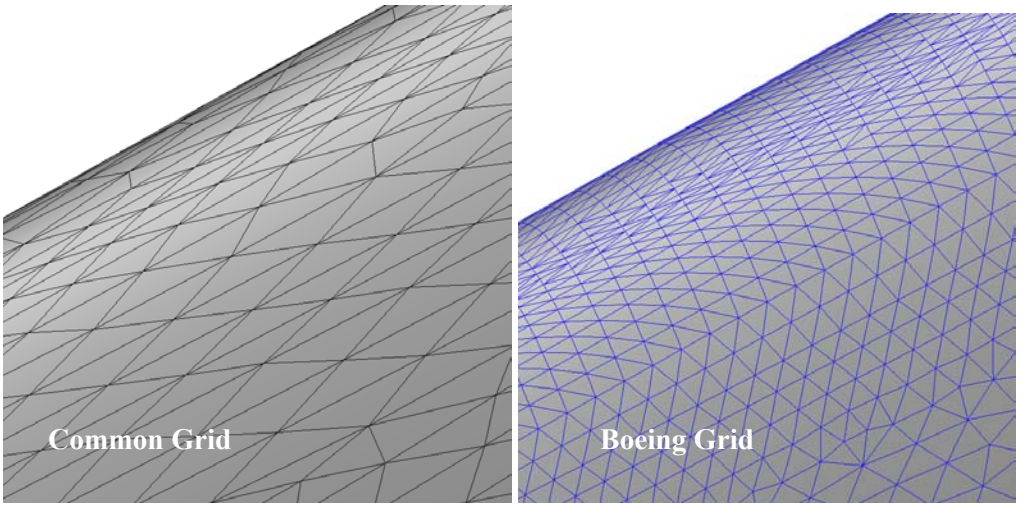

Figure 12-5: Comparison of Surface Meshes Near the Wing Leading Edge.

The volume portion of the Boeing mesh was generated in AFLR and consists of a semi-structured boundary layer extrusion connected to an isotropic tetrahedral grid. The extrusion used a 0.0003 inch initial spacing at the wall to yield a y+ of approximately 1 across the five flight conditions. The initial spacing grew geometrically with an initial growth ratio of 1.2 ending at a 1.8 maximum growth ratio. Extrusion terminated when the prisms achieved an aspect ratio near unity. The combination of the initial viscous spacing, growth rate parameters, and surface spacing produced approximately 15 prism layers. The resulting volume grid had 19.3 million cells. This mesh will be referred to as the Boeing baseline mesh.

A BCFD solution was generated on the Boeing baseline mesh at Flight Condition 7. Contours of the predicted surface pressure coefficient and normalized total pressure ratio at several fuselage station cuts are shown in Figure 12-6. The three primary vortices evident in the common grid solution are once again visible in the Boeing baseline mesh solution. Compared to the solutions on the common grid presented in Figure 12-3, the suction peak along the primary vortices is slightly more pronounced and the total pressure loss in the vortex core persists further downstream indicating less dissipation of the vortex.

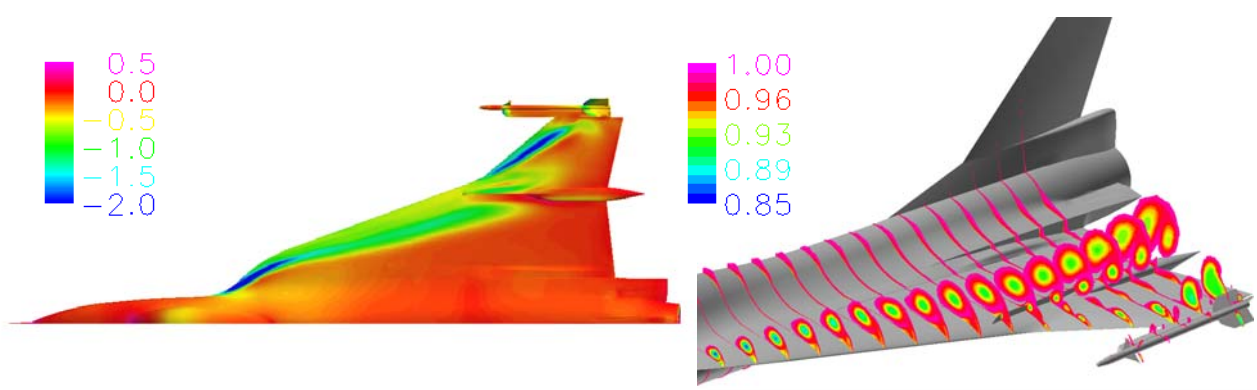

Figure 12-6: Surface Pressure Coefficient and Total Pressure Ratio Contours on Boeing Baseline Grid at Flight Condition 7 with the SA Turbulence Model.

BCFD surface pressure predictions on the Boeing baseline mesh are indicated by the solid red line in Figure 12-3. Compared to the common mesh results, the surface pressure compares better with the test data near the wing leading edge. The most noticeable difference from the common grid results is the presence of a secondary vortex clearly visible at BL stations 70 through 95. Although there is not an appreciable change in the magnitude of the pressure peak compared with the common grid results, the location of the peak has moved aft and correlates better with the test data. The primary vortex outboard of the wing fence is much stronger in the Boeing mesh results. This is evident in the higher surface suction peak at BL station 153.5. The prediction deviates from the test data about the mid-chord location of BL 184.5. This BL is close to the tip missile. Examining the surface pressure contours in Figure 12-6 it appears that the track of the primary vortex is influenced by an interaction with the wing tip missile launcher. Predicted velocity profiles on the Boeing mesh at rake locations 4 through 7 are indicated by the solid red line in Figure 12-4. The improvement in the velocity profiles is most likely a result of the increased mesh resolution in the boundary layer and a better pressure prediction at the boundary layer edge.

Although the Boeing baseline mesh improved the location of the primary vortex over the common mesh, the magnitude of the suction peak is still under predicted. One possible explanation for this may be the off-body mesh resolution near the vortex core. As the primary vortex grows and convects downstream, it moves away from the surface and into the coarser tetrahedral portion of the volume mesh. This decrease in mesh resolution corresponds to an increase the numerical dissipation and may lead to a premature reduction in the predicted vortex strength and a smearing of the pressure suction peak on the surface.

To help assess the impact of the off body grid resolution, a new volume mesh was created with increased resolution along the vortex core path. The mesh was refined by placing grid resolution sources along traces of the three primary vortex cores predicted by the BCFD solution. This adapted grid utilized the same surface grid as the baseline Boeing grid, but the addition of sources increased the size of the volume grid to 23.3 million cells. The mesh resolution at BL cuts through the adapted and non-adapted volume meshes at BL 70 and BL 153.5 is shown in Figure 12-7 and Figure 12-8. The increase in off body resolution along the vortex path inboard of the wing fence is evident in Figure 12-7. Adaptation to the vortex core outboard of the fence had less impact on the mesh since the baseline volume mesh was already relatively dense in this area.

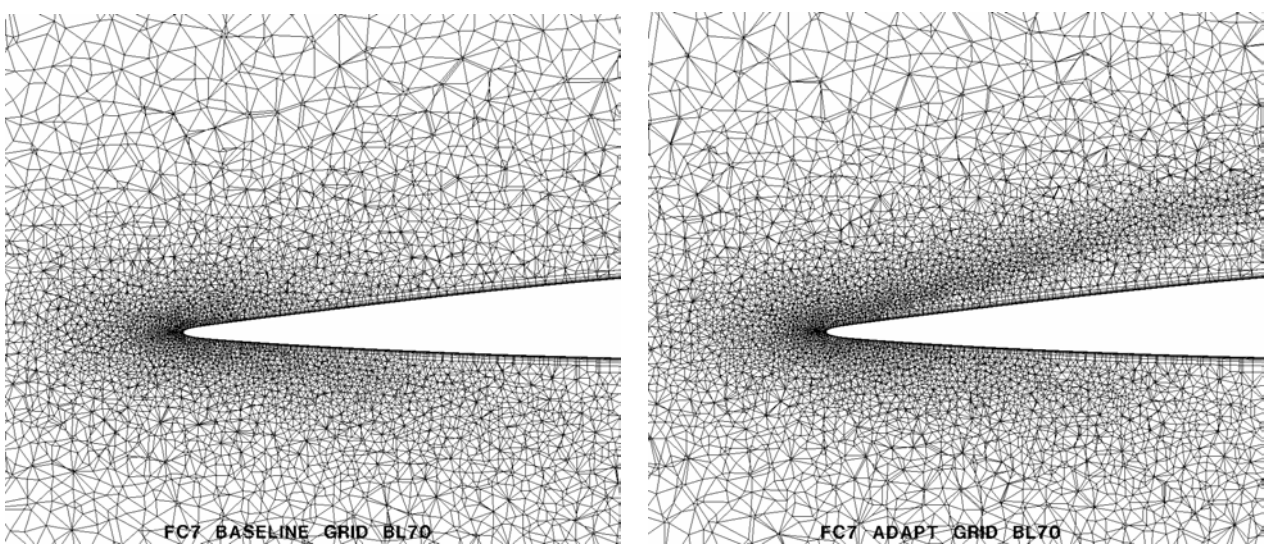

Figure 12-7: Cut Through Boeing Baseline and FC7 Adapted Grids at BL 70 Inches.

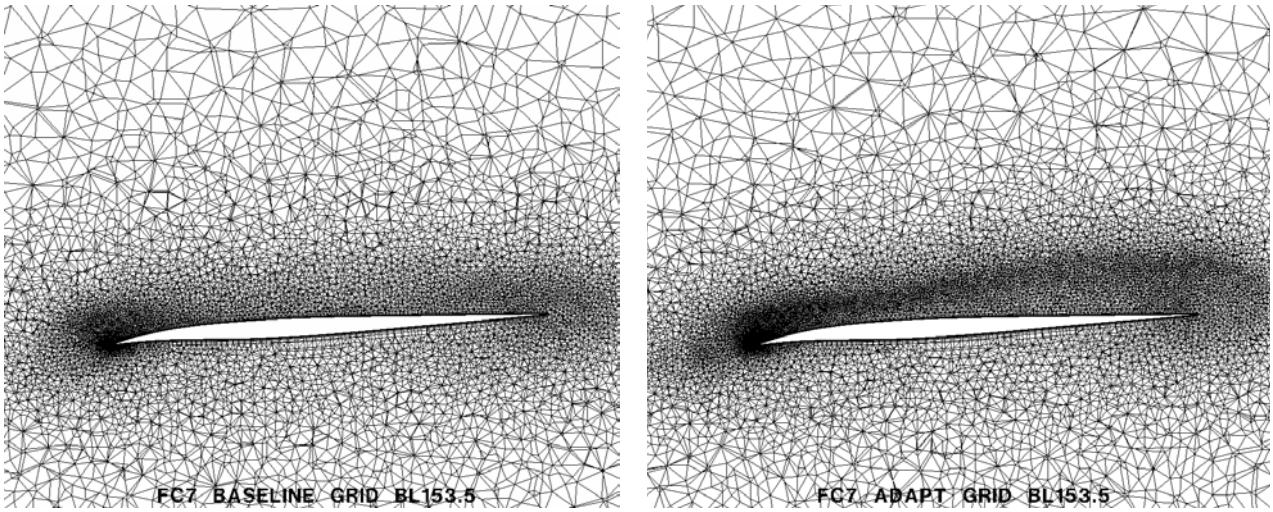

Figure 12-8: Cut Through Boeing Baseline and FC7 Adapted Grids at BL 153.5 Inches.

A BCFD solution was generated on the adapted mesh at Flight Condition 7. Contours of the predicted surface pressure coefficient and normalized total pressure ratio at several fuselage station cuts are shown in Figure 12-9. The contours inboard of the wing fence are similar to the non-adapted results shown in Figure 12-6. The primary vortex suction peak is slightly better defined in the surface pressure contours for the adapted grid solution. Outboard of the wing fence, the primary vortex in the adapted grid solution turns downstream earlier than the results on the non-adapted grid. The interaction with the tip missile launcher is slightly less pronounced.

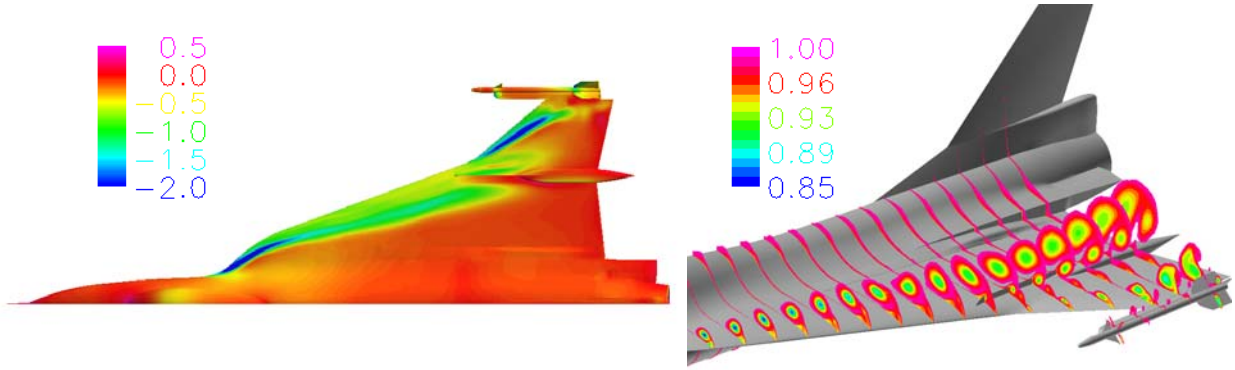

Figure 12-9: Surface Pressure Coefficient and Total Pressure Ratio Contours on Boeing Adapted Grid at Flight Condition 7 with the SA Turbulence Model.

Surface pressure results on the Boeing adapted mesh are indicated by a dashed red line in Figure 12-3. Adaptation of the off body mesh near the vortex core resulted in a small but noticeable improvement in the surface pressure predictions at the inboard wing BL stations of 55 through 95. The primary change is a slight increase in the suction peak. The reduced interaction with the tip missile launcher changes the surface pressure at BL station 184.5 from the baseline grid, but the impact of the outboard vortex with the tip missile launcher still results in a pressure peak that is not evident in the test data. At this flight condition, the vortex remains relatively close to the surface for much of the track over the wing. The mesh resolution in this area is dominated by the surface mesh size thereby reducing the impact of the volume mesh adaptation. One lesson

learned from this study is that effective adaptation of the mesh for vortical flow computations, particularly when the vortices remain close to the surface, requires adaptation of the surface mesh in addition to the volume mesh.

Boundary layer velocity profiles predicted on the adapted mesh are represented by the dashed red line in Figure 12-4. The profiles from the adapted and non-adapted grid solutions are very similar with a slight improvement in the adapted mesh profiles at Rakes 4 and 7. Only the tetrahedral elements of the Boeing mesh were affected by the adaptation and the prismatic elements across the boundary layer are unchanged between the adapted and baseline meshes. The differences in the velocity profiles are therefore a result of the minor changes in the pressure distribution outside of the boundary layer at the four rake locations.

Turbulence plays an important role in the dissipation and entrainment of vortical flows. It is not surprising therefore that the choice of turbulence model can have a big impact on the quality of the CFD results. The BCFD solutions on the AVT common, Boeing baseline, and Boeing adapted grids were computed using the Spalart-Allmaras (SA) turbulence model. Previous computations have shown that the SA model over predicts the production of turbulence in the off body vortex core. A modification that reduces the turbulence production based on the local rotation of the flow helps to minimize this affect [12-9]. The rotational correction has also been shown to under predict the production of turbulence in the secondary vortex and was therefore not used in the BCFD computations.

To assess the impact of the choice of turbulence model, a BCFD solution was computed on the Boeing adapted mesh using the Menter SST two-equation turbulence model [12-10]. This model utilizes a combination of the k-ω formulation in the boundary layer and a k-ε formulation outside the wall bounded regions. The SST model has been shown to accurately predict off body flow-field features. Contours of the surface pressure coefficient and total pressure ratio at fuselage station cuts from the SST computation are shown in Figure 12-10. Compared to the SA turbulence model results on the same mesh, the strength of the vortex core is reduced with the SST turbulence model. This is evident from the reduction in the total pressure loss in the vortex core. BL station cuts of the surface pressure for the SST computations are indicated by blue dashed lines in Figure 12-3. Consistent with the reduced vortex strength indicated by the total pressure cuts, the surface pressure results show a reduced suction peak along the vortex core. This reduction in the vortex core strength with the SST model indicates an increase in dissipation of the vortex relative to the SA results. These results are contrary to what was anticipated and they are inconsistent with comparisons of these two models on other configurations using structured grids. As a result of this study, the implementation of the SST model on unstructured grids is being investigated.

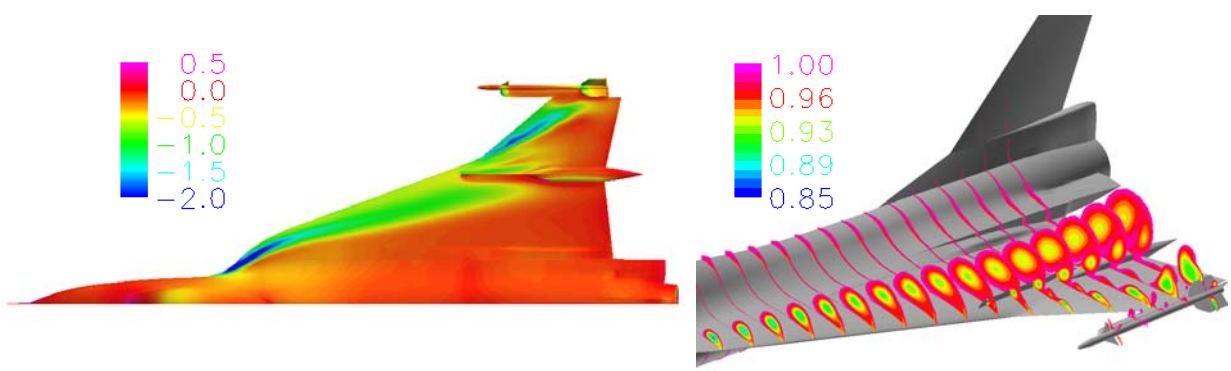

Figure 12-10: Surface Pressure Coefficient and Total Pressure Ratio Contours on Boeing Adapted Grid at Flight Condition 7 with SST Turbulence Model.

Predicted velocity profiles from the SST results are shown by dashed blue lines in Figure 12-4. The profiles are similar to the SA results with the SST solution indicating a slight increase in the velocity gradient at the wall. Based on these results, the SA turbulence model provides better results for vortex dominated flows.

The sequence of BCFD solutions performed at Flight Condition 7 was repeated at Flight Condition 25. This consisted of solutions on the baseline Boeing mesh, an adapted Boeing mesh, and solutions with SA and SST turbulence models. The conditions at FC25, Mach 0.242, 19.84 degrees angle of attack and a Reynolds number of 32.22 million, are extremely challenging for CFD analysis. At this flight condition, the vortices are much stronger and the physical flow field is characterized by a larger degree of unsteadiness. Application of a steady state Reynolds Averaged Navier-Stokes (RANS) solution at these conditions may not be satisfactory. To measure the impact of time accuracy, an unsteady computation was also performed at this flight condition.

The computed surface pressure is compared with test results at several BL cuts in Figure 12-11. Predicted surface pressure and fuselage station cuts of the total pressure ratio are shown in Figure 12-15. The general trends observed at FC 7 are seen again at this flight condition. Overall, the CFD results agree well with the test data. There are details of the flow field, particularly near the vortices, were the CFD and test results differ. The predicted strength of the primary vortex compares favourably with the test results at most of the BL stations. However, the predicted suction peak is broader than the test data indicate. The steady-state CFD results show a very weak indication of a secondary vortex while the suction peak from the secondary vortex is very pronounced in the test data. These features are particularly noticeable just inboard of the fence at BL stations 80 and 95. Unlike the FC7 results, the SA and SST turbulence models provide very similar solutions at this flight condition. While the SA results in general are slightly closer to the test data, the spread between the two turbulence models is less pronounced than it was at FC7. This may be an indication that the vortex formation and tracking at high angle of attack is less influenced by turbulence effects and more dominated by convection. Because the SST results were comparable to the SA model, the solution on the adapted mesh was computed using the SST turbulence model. There is almost no difference between the adapted and non-adapted mesh solutions. As with the lack of turbulence model sensitivity, this may be an indication that the large strong vortices are primarily dominated by convection and that numerical dissipation plays a secondary role in the vortex prediction.

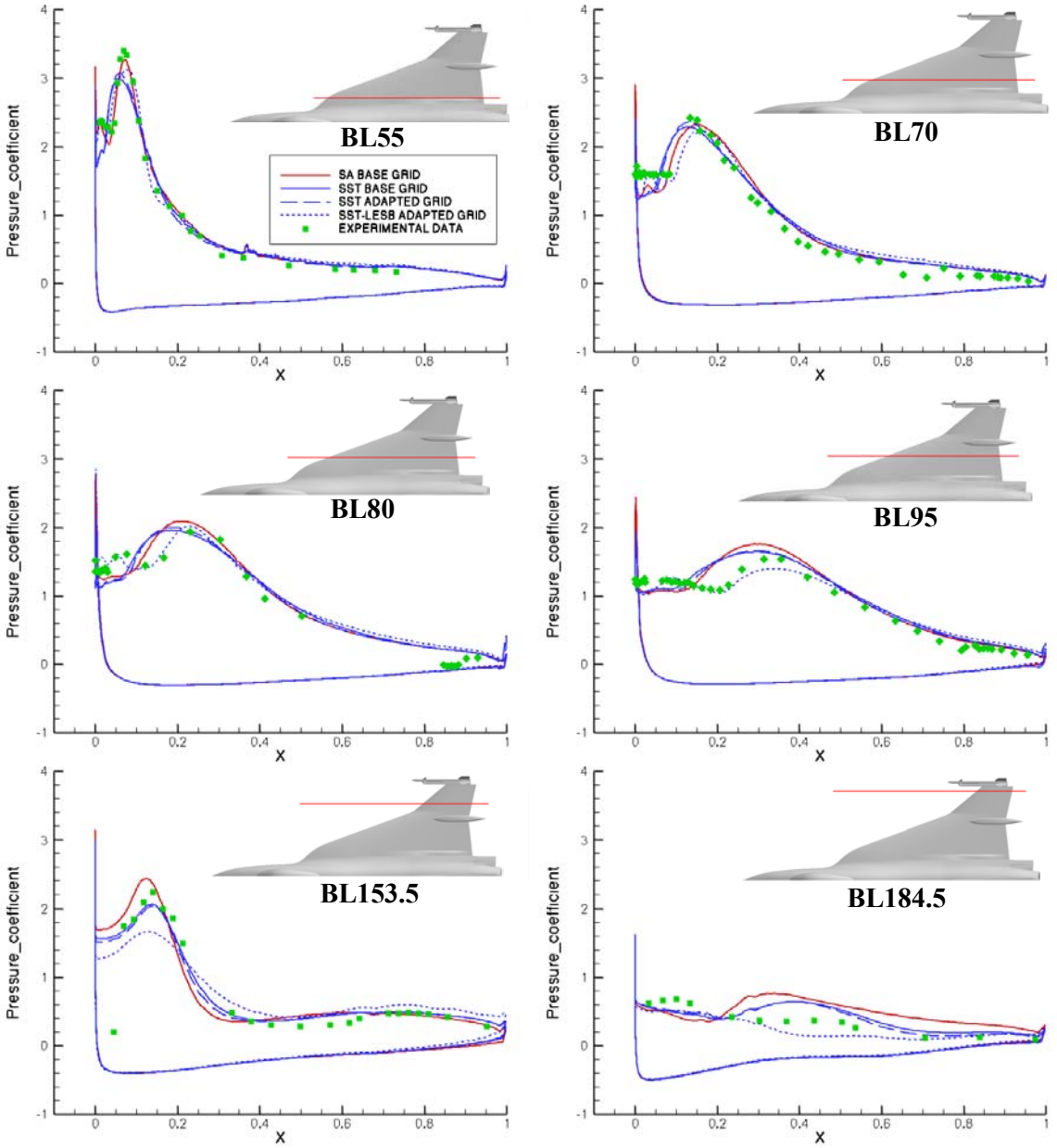

Figure 12-11: Comparison of Computed Surface Pressure Coefficient for Several Butt-Line Cuts at Flight Condition 25.

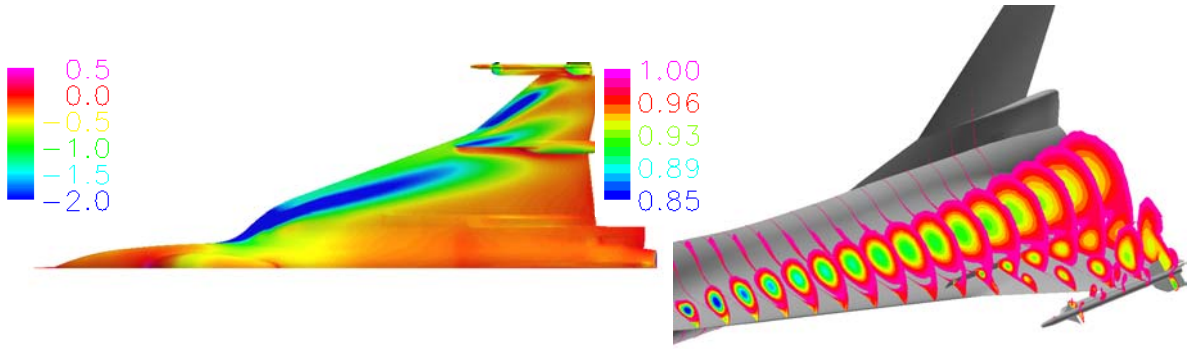

Figure 12-12: Surface Pressure Coefficient and Total Pressure Ratio Contours on Boeing Baseline Grid at Flight Condition 25 with the SA Turbulence Model.

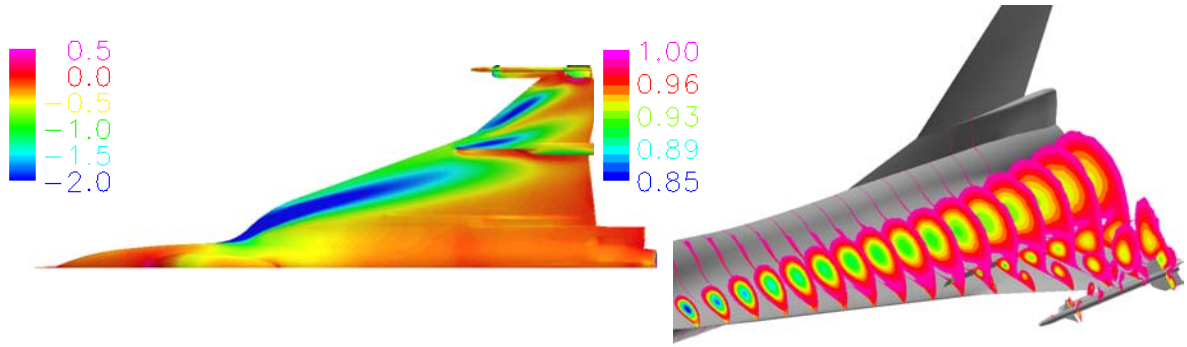

Figure 12-13: Surface Pressure Coefficient and Total Pressure Ratio Contours on Boeing Baseline Grid at Flight Condition 25 with the SST Turbulence Model.

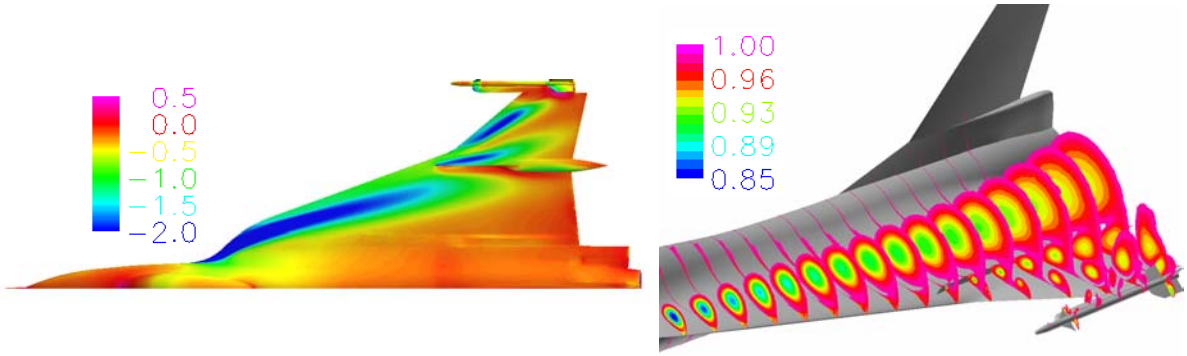

Figure 12-14: Surface Pressure Coefficient and Total Pressure Ratio Contours on Boeing Adapted Grid at Flight Condition 25 with the SST Turbulence Model.

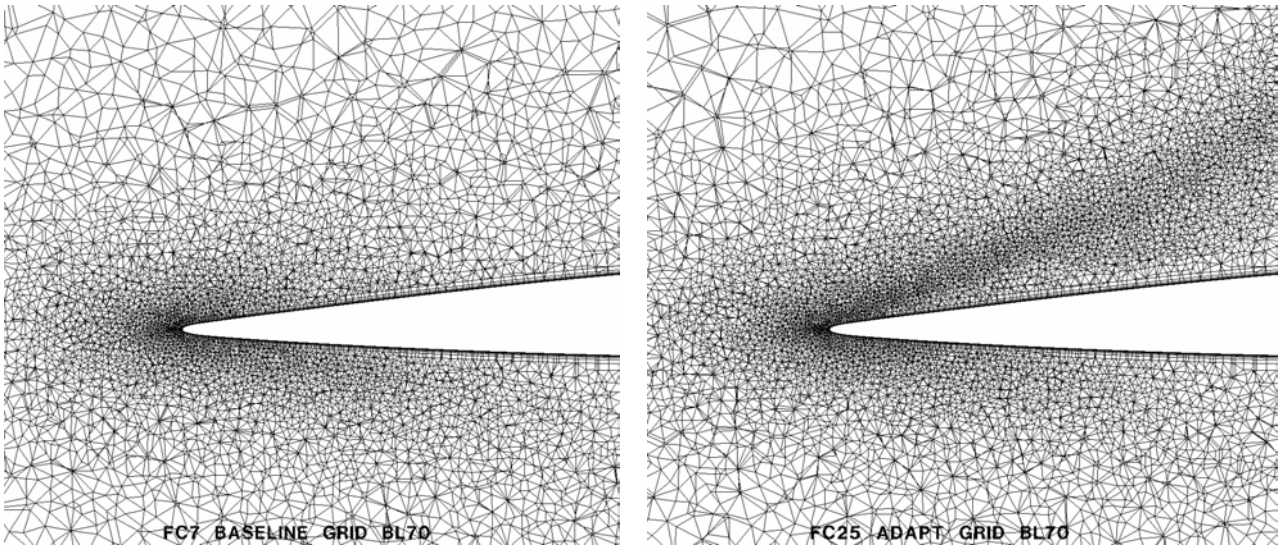

Figure 12-15: Cut Through Boeing Baseline and FC25 Adapted Grids at BL 70 Inches.

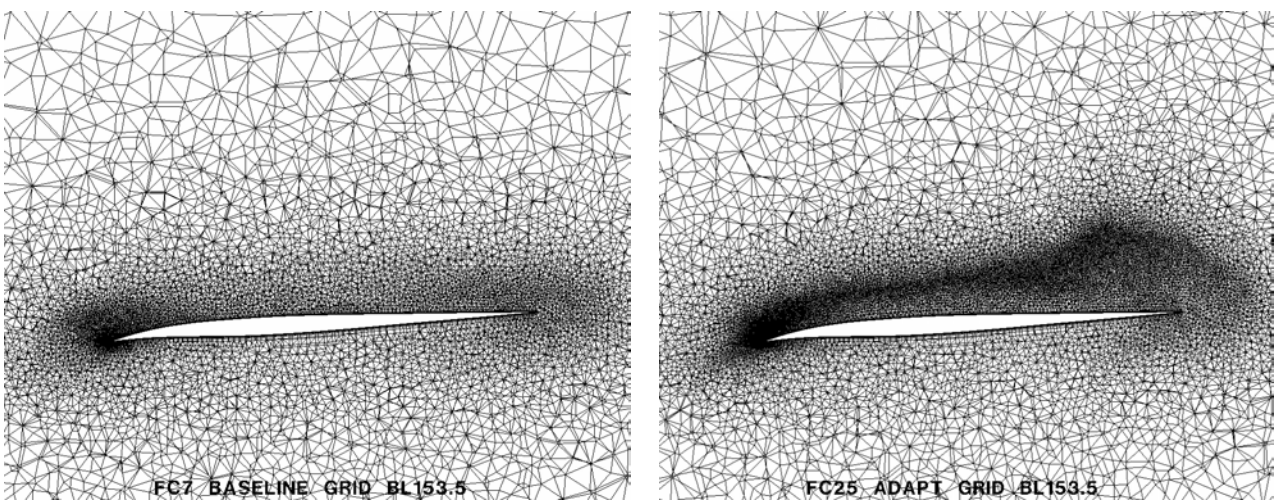

Figure 12-16: Cut Through Boeing Baseline and FC25 Adapted Grids at BL 153.5 Inches.

An assessment of the impact of time accurate computation was made by computing an unsteady BCFD computation using the hybrid SST/LESb turbulence model. The SST/LESb model was developed for unsteady massively separated flows [12-11]. The idea for the balanced Large Eddy Simulation (LESb) stems from the Detached Eddy Simulation of Spalart [12-12]. The distinction between various RANS turbulence models, and LES models, comes in the definition of the turbulent viscosity (μ_t). For RANS models the turbulent viscosity is related to a turbulent length scale and the turbulent kinetic energy per unit mass (k): $\mu_t = \bar{\rho} C_\mu l_\varepsilon \sqrt{k}$.

The key to the LESb model is a re-formulation of the turbulent viscosity based on the kinetic energy of the unresolved scales (k). $\mu_t = \bar{\rho} C_\mu C_B \Delta \sqrt{k}$.

Where C_μ is added for consistency with the two equation formulation and the coefficient C_B is added to allow refinement of the model.

LES formulations generally rest on a smooth transition between the modelled to unresolved scales of turbulence. Such a transition implies an isotropic resolution of the smallest resolved scales. This resolution requirement is generally the limiting factor of the scales and accuracy of the cases modelled and of the complexity of the flows that can be affordably computed. The LESb model will try to remove this restriction by allowing stretched grids to model high mean shear where the grid resolution required to capture the shear stress is greater than that required to capture the unsteadiness of interest. Of course, the stretched grids will not be able to resolve isotropic turbulence at these scales, so the model will rely on proven two-equation turbulence models as our best attempt to model the turbulence on this scale.

The two equation RANS models use *k* to represent all of the unsteady fluctuations, while the LES models use *k* to represent only the spatial average of the fluctuations within a filter width. For the balanced LES model (LESb), we define a new length scale l_B: $l_B = \min(l_\varepsilon, C_B\Delta)$ and the LESb model represents the turbulent viscosity as: $\mu_t = \bar{\rho} C_\mu l_B \sqrt{k}$.

For unresolved length scales ($\Delta >> l_\varepsilon$) the model reverts to the standard two equation model. However, for resolved length scales ($\Delta << l_\varepsilon$) the model reverts to the LES model, and as the resolved length scale goes to zero (full resolution of all pertinent scales) the model approaches a Direct Numerical Simulation (DNS) of turbulence. To define Δ consistently with resolving the small eddies, for isotropic grids, we could easily set $\Delta = (Volume)^{1/3} = (1/J)^{1/3}$, where J is the Jacobian of the grid transformation. For stretched grids, we assume that the smallest resolved eddies should be roughly isotropic and so must be resolved in all three coordinate directions, and in time. Thus we set: $\Delta = \max(dx, dy, dz, u * dt, \sqrt{k} * dt)$.

The limiting length scales based on time step represent the scales based on convection velocity and SGS turbulence respectively. These scales are included to ensure that there is sufficient time resolution to resolve the captured physical phenomena. That is, if the time steps are too large, the unsteady phenomena cannot be resolved, and the RANS model should be used.

The BCFD unsteady solution was run with a Newton time stepping algorithm at a time step of 0.0005 seconds. The steady state RANS solution was used at the initial state and a total of 10,000 time steps were computed in the unsteady result. The solution over the last 2000 time steps was averaged for comparison with test data. The time average surface pressure is represented by the blue dotted line in Figure 12-11. Contours of surface pressure and total pressure ratio from the time averaged solution are shown in Figure 12-17. The total pressure loss in the vortex core is more pronounced and persists further down stream than for the RANS results. Also noticeable in the surface pressure and total pressure contours is the presence of a secondary vortex. The vortices on the outboard wing panel are reduced in strength from the steady state results. The comparison of the surface pressure with test data in Figure 12-11 is improved, particularly near the secondary vortex at BL stations 55 through 95. The location of the suction peak associated with the primary vortex core at these BL stations is also shifted aft and matches the test data better than for the steady state results.

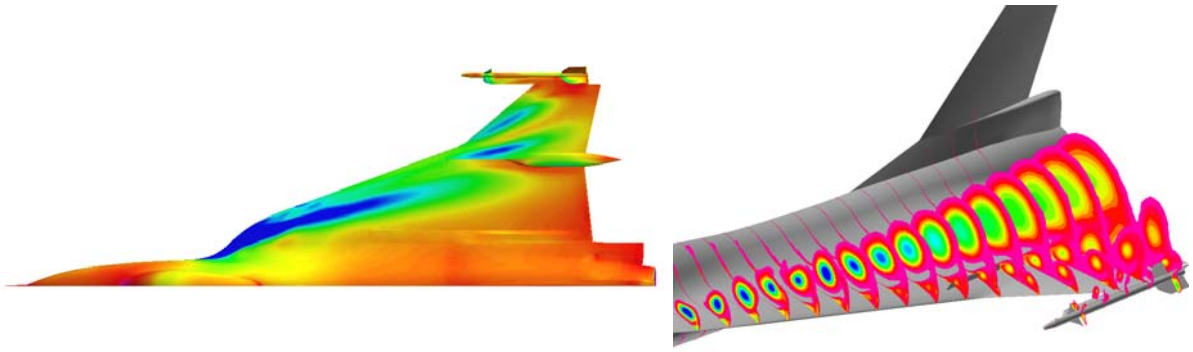

Figure 12-17: Time Average Surface Pressure Coefficient and Total Pressure Ratio Contours on Boeing Adapted Grid at Flight Condition 25 with the LESB Turbulence Model.

12.5 SUMMARY AND CONCLUSIONS

BCFD computations were performed on the F-16 XL configuration at high angles of attack. Results were compared with surface pressure and boundary layer measurements taken in flight. Several studies were performed to assess the impact of grid resolution, turbulence model and time accuracy on the CFD results.

Given the complex nature of the flow field, the BCFD predictions match the test data very well. The BCFD computations accurately predict the formation and propagation of three primary vortices along the locations given by the test data. The resolution of the surface mesh around the leading edge and along the vortex core was found to be an important factor in the accurate prediction of the suction peak. Grid adaptation improved the prediction of vortex strength. The close proximity of the vortices to the surface reduced the effectiveness of the volume only adaptation procedure used in this study. Effective adaptation to wing vortices requires adaptation of the surface mesh in addition to the volume mesh. Of the two turbulence models used in this study, the Spalart-Allmaras turbulence model provided better results for a steady-state RANS solution. The steady-state RANS solutions tended to under predict the strength of the secondary vortex. Accuracy of the computations was improved by modelling the flow with and unsteady computation and a LESb turbulence model. Unsteady simulations using the SST-LESb turbulence model provided the best accuracy across all of the computed flight conditions.

12.6 REFERENCES

[12-1] Del Frate, J.H., Fisher, D.F. and Zuniga, F.A.: *In-Flight Flow Visualization with Pressure Measurements at Low Speeds on the NASA F-18 High Alpha Research Vehicle*, NASA TM-101726, October 1990.

[12-2] Meyn, L.A., Lanser, W.R. and James, K.D.: *Full-Scale High Angle-of-Attack Test of an F/A-18*, AIAA 92-2676.

[12-3] Lamar, J.E., Obara, C.J., Fisher, B.D. and Fisher, D.F.: *Flight, Wind-Tunnel, and Computational Fluid Dynamics Comparison for Cranked Arrow Win (F-16XL-1) at Subsonic and Transonic Speeds*, NASA/TP-2001-210629, February 2001.

[12-4] Lamar, J.E. and Obara, C.J.: *Review of Cranked-Arrow Wing Aerodynamics Project: Its International Aeronautical Community Role*, AIAA-2007-487, January 2007.

[12-5] Rizzi, A., Badcock, K.J., Jirásek, A. and Boelens, O.J.: *What was Learned from Numerical Simulations of F-16XL (CAWAPI) at Flight Conditions*, AIAA-2007-683, January 2007.

[12-6] Marcum, D.L.: *Advancing-Front/Local-Reconnection (AFLR) Unstructured Grid Generation,* Computational Fluid Dynamics Review, World Scientific – Singapore, 1998, p. 140.

[12-7] Mani, M., Cary, A. and Ramakrishnan, S.V.: *A Structured and Hybrid Unstructured Grid Euler and Navier-Stokes Solver for General Geometry*, AIAA-2004-524, January 2007.

[12-8] Boelens, O.J., Görtz, S., Morton, S. and Fritz, W.: *Description of the F16-XL Geometry and Computational Grids Used in CAWAPI*, AIAA-2007-488, January 2007.

[12-9] Spalart, P.R. and Shur, M.L.: *On the Sensitization of Turbulence Models to Rotation and Curvature*, Aerospace Science and Technology, No. 5, 1997, pp. 297-302.

[12-10] Menter, F.R.: *Improved Two-Equation K-ω Turbulence Models for Aerodynamic Flows*, NASA TM 103975, October 1992.

[12-11] Bush, R.H. and Mani, M.: *A Two-Equation Large Eddy Stress Model for High Sub-Grid Shear*, AIAA-2001-2561.

[12-12] Spalart, P.R., Jou, W.H., Strelets, M. and Allmaras, S.R.: *Comments on the Feasibility of LES for Wings, and on a Hybrid RANS/LES Approach*, 1st AFOSR Int. Conf. on DNS/LES, August 4-8, 1997, Ruston, LA.